

**MICRO-DISPENSER BASED OPTICAL  
PACKAGING SCHEME FOR  
GRATING COUPLERS**

by

S M Zia Uddin

A thesis submitted to the Faculty of the University of Delaware in partial fulfillment of the requirements for the degree of Master of Science in Electrical and Computer Engineering

Summer 2023

© 2023 S M Zia Uddin  
All Rights Reserved

**MICRO-DISPENSER BASED OPTICAL  
PACKAGING SCHEME FOR  
GRATING COUPLERS**

by

S M Zia Uddin

Approved: \_\_\_\_\_  
Tingyi Gu, Ph.D.  
Professor in charge of thesis

Approved: \_\_\_\_\_  
Jamie D. Phillips, Ph.D.  
Chair of the Department of Electrical and Computer Engineering

Approved: \_\_\_\_\_  
Levi T. Thompson, Ph.D.  
Dean of the College of Engineering

Approved: \_\_\_\_\_  
Louis F. Rossi, Ph.D.  
Vice Provost for Graduate and Professional Education and  
Dean of the Graduate College

## **ACKNOWLEDGEMENTS**

I would like to thank my advisor, Dr. Tingyi Gu for her guidance, patience and support during my research. I want to thank all the members of our research group. I also want to thank the members of our collaboration. I want to thank staff members from UD Nanofabrication facility. I would like to thank my parents and sister for their love and encouragement. I am also grateful to my friends, G M Shashi, S M Jahadun Nobi Apon, Saiful Tarek and so on.

## TABLE OF CONTENTS

<b>LIST OF TABLES .....</b>	<b>v</b>
<b>LIST OF FIGURES .....</b>	<b>vi</b>
<b>ABSTRACT.....</b>	<b>viii</b>
 <b>Chapter</b>	
<b>1 INTRODUCTION.....</b>	<b>1</b>
<b>2 BACKGROUNDS .....</b>	<b>4</b>
2.1 Silicon Photonics for Optical devices .....	4
2.2 Grating Coupler .....	4
2.3 Waveguide-to-fiber Coupler fabricated through DLW method.....	8
2.4 Optical Packaging .....	8
2.5 Precision micro-dispensing Process.....	11
2.6 Micro-lens array through ink-jet printing .....	14
2.7 Far-field Projection .....	15
<b>3 OPTICAL PACKAGING THROUGH GRATING COUPLER.....</b>	<b>19</b>
3.1 Design principle of Grating Coupler.....	19
3.2 Micro-dispenser-based lens printing on grating coupler .....	20
3.3 Micro lens dimension calculations through Profilometer .....	21
3.4 Experimental Analysis .....	23
3.4.1 Coupling for incoming beam .....	23
3.4.2 Coupling for outgoing beam (Far-field projection) .....	27
<b>4 CONCLUSIONS AND PERSPECTIVES .....</b>	<b>30</b>
<b>REFERENCES.....</b>	<b>32</b>

## LIST OF TABLES

2.1 Performance comparison of some exemplary grating couplers .....	7
---	---

## LIST OF FIGURES

2.1	Schematic structure for a 1D grating coupler (GC) with linear waveguide taper and key parameters: period $\Lambda$ , fiber tilt angle $\theta$ , varying taper width $W$ and taper angle $\theta_{\text{taper}}$ . [18].....	5
2.2	(a) Loss channels in input and output coupling; (b) wave-vector diagram for fiber-to-chip coupling; and (c) wave-vector diagram for chip-to-fiber perfectly vertical coupling,[18].....	5
2.3	(a)Schematic drawing of different types of couplers: Uniform grating in (a) SOI with air top cladding, (b) SOI with oxide top cladding, (c) SOI with bottom Si/SiO <sub>2</sub> mirror. In (d), a grating coupler with varying groove widths is shown. Dark gray represents Si and light gray SiO <sub>2</sub> . [19] .....	6
2.4	(a) Rendering of a polymer coupler (blue) attached to a silicon nitride waveguide (orange). The double-square-markers used for alignment are also shown. (b) Rendering of the hybrid photonic circuit for carrying out transmission tests. A fiber array with a pitch of 250 $\mu\text{m}$ is placed over the couplers. Both couplers are connected by a silicon nitride single mode waveguide. (c) SEM-micrograph of a fabricated coupler realized by DLW. (d) SEM-micrograph of a photonic chip with several devices illustrating scalable fabrication of hybrid 3D-planar photonic circuits. [20] .....	8
2.5	Various packaging technologies available through PIXAPP.....	9
2.6	Schematic of packaging the first 3 assembly strands on PIC. The (1) deals with EICs, (2) with microlenses, and (3) with the MOB .....	10
2.7	MOB setup connected with ball lens and prism .....	11
2.8	Sequential process of the making of droplet (a) (a) Preparatory position (no droplet created), (b) Dispensing position (droplet in-progress), (c) Returning position (droplet created). [44] .....	12
2.9	Force analysis of the droplet at the tip of the injector. [44].....	13
2.10	(a) Complete installation of microdispensing system (b) Microdispensing installation in X_Y table; (1) injector, (2) workpiece, (3) piezoelectric actuator, (4) liquid container, (5) X-axis, (6) Y-axis. [44] .....	13

2.11 (a–e) Illustrative steps of the micro platforms fabrication process; (f) MLA inkjet printing process .....	14
2.12 (a)Schematic of a 2D OPA (b) Operational principle of phased array [22] .....	16
2.13 Schematic diagram of far field beam with different spacing and aperture condition.[22].....	17
3.1 Grating coupler on SOI substrate.....	19
3.2 Hemi-spherical lens on grating coupler .....	20
3.3 (a) Top view of micro-lens printed on grating coupler captured by camera in microdispensing system. (b) Perspective view of the lens on grating coupler captured by confocal laser microscope system. [53] .....	20
3.4 (a) Schematic diagram of the devices' cross-section. The contact angle ( $\alpha$ ) on the interface determines the numerical aperture of the lens. (b) Measured spherical radius R and versus in-plane radius r measured across the 10 micro-lenses produced by the dispenser. Right y-axis: correspondent numerical radius .....	21
3.5 $\mu$ lens modified fiber-chip coupling spectra. (a) Cross-sectional schematics indicating the incident angle $\theta$ . (b) Transmission spectra versus incident angle for the apodized grating coupler defined on SOI and (c) same device with $\mu$ lens.[53] .....	23
3.6 (a) Peak transmission versus incident angle at the optimal transmission wavelength in b and c for without (blue) and with $\mu$ lens (orange). (b) The extracted full- width half maximum bandwidth of transmission spectra versus incident angle for both conditions. [53] .....	24
3.7 Measured optical characteristics. (a) Numerically predicted and (b)measured transmission spectra of the $\mu$ lens atop grating coupler with (orange) and the same design without $\mu$ lens (blue), at the incident angles of $7^\circ$ (dashed) and $14^\circ$ (solid curves). (c) Peak transmission of $\mu$ lens atop grating couplers versus the height of the $\mu$ lens for the incident angle of $7^\circ$ (blue) and $14^\circ$ (orange) .....	25
3.8 $\mu$ lens modified far field projection for dispersion-based beam steering. (a) Cross-sectional view of the grating coupler with in-waveguide excitations, and (b) after adding the $\mu$ lens ( $R=100\ \mu\text{m}$ , $h=2.75\ \mu\text{m}$ ). (c) Incident wavelength-dependent far-field projection, for bare grating coupler (blue) and with $\mu$ lens (yellow). (d) Selective far field project at the input laser wavelength of $1.50\ \mu\text{m}$ (at the distance of 1m).....	27
3.9 Incident wavelength-dependent far-field projection, (a) misalignment in the x- direction, and (b) y direction after adding the $\mu$ lens ( $R=100\ \mu\text{m}$ , $h=2.75\ \mu\text{m}$ .....	28

## **ABSTRACT**

In this thesis, a design concept has proposed where several micro-lenses can be printed on grating couplers through micro-dispenser-based printing method. This method not only ensures excellent efficiency but is also feasible for easy and fast fabrication process. The author demonstrates the optical property of the proposed device in terms of both incoming and outgoing beam to the device. The device provides high angle tolerance as well as a remarkable resolution in the far-field.

## **Chapter 1**

### **INTRODUCTION**

In integrated optical systems, coupling light between on-chip waveguides, fibers and free-space optical elements plays a very important role and can also be a solution to packaging challenges [52]. This sector holds tremendous potential having numerous applications such as quantum optics [23,24], optical phased array for beam steering in free space [25], biosensing [26,27], optical trapping [28-30] to name a few.

Silicon-on-insulator (SOI) wafers can act as an ideal platform for nanophotonic waveguide circuits. Standard Single mode fiber comprises a mode field diameter of 10  $\mu\text{m}$  at 1550 nm whereas the waveguide has a dimension of few hundreds of nanometers. As a result, a large modal mismatch occurs that makes the coupling challenging. In-plane (butt) edge coupling and Off-plane (vertical) grating coupling can be the solutions for this problem.

Inverse tapered waveguide is used in edge coupler and with the gradual decrease of taper towards the edge, it tends to confine less light that results in larger mode size. Higher coupling efficiency and large bandwidth are the major attributes to this coupler, but it is less feasible for production. [18]

On the other hand, grating coupler can be placed anywhere on the chip which makes it more feasible for production. When an off-plane wave vector direction of light falls upon the grating coupler it becomes the in-plane light directed towards the waveguide. The drawbacks are lower coupling efficiency, sensitivity to polarization and wavelength. [18] Using additional cladding layer can enhance the efficiency of this coupler [19] while lens on a polymer coupler can shape the beam [20]. Combining these two functionalities, it can be said that use of lenses as cladding layer can improve the coupling efficiency while controlling the beam direction. Therefore, optical packaging can be realized as packaging refers to the connection between PIC and outside world [31]. A Direct Laser Method (DLW) method has been implemented to construct freeform optical coupler with lens [20] that enables the optical packaging with high contrast [53]. Ink-Jet printing also acts as an alternative additive manufacturing process (AM) to fabricate micro-lens array with high throughput [20, 53].

In this thesis, a Micro-dispenser-based method has been proposed which not only provides easy fabrication but also faster than other AM counterparts. Hemi-spherical shaped micro-lenses can be placed on top of the apodized grating coupler as a cladding layer that improves efficiency as well as demonstrates better angle tolerances for the input beam. Additionally, the same structure can be used for the outgoing beam and far-field projection characteristics both for with and without microlenses have been studied here.

Based on microdispensing method the author develops an idea to couple light more efficiently. In chapter 2, the author introduces the background of the research. In chapter 3,

the author presents the different optical characteristics of grating couplers both for with and without micro-lenses. We can achieve angle tolerance for incoming light which has been verified both with simulation and measurement. Additionally, for outgoing beams, different wavelengths have been analyzed for projection in the far-field. This device can be used for both incoming and outgoing light which eventually has broadened its potential for different photonic applications.

This work is done in collaboration with Ellen Gupta, Masudur Rahim, Zi Wang, Yang Du, Kaleem Ullah, Craig B. Arnold, Mark Mirotznik, and Tingyi Gu. It is published as” Micro-dispenser-based optical packaging scheme for grating couplers”, Optics Letters, 2023.

## **Chapter 2**

### **BACKGROUNDS**

#### **2.1 Silicon Photonics for Optical devices**

Silicon photonics has revolutionized optics in the last two decades. One of the key attributes to this is that the dimensions are typically an order of magnitude smaller compared to optical fiber devices. There is a significant difference in dimension between the fiber and chip. The issue can be addressed through two main fiber-to-chip interface approaches namely, in-plane and out-of-plane couplers.[2] Utilizing silicon (Si) waveguides as a fundamental component [3-5], different optical parts can be executed, for example, directional couplers [6], Y-branches [7], conveyed waveguide Bragg gratings [8], and arrayed waveguide gratings (AWGs) [9], Mach-Zehnder interferometers [10] and ring resonators [11,12] have been illustrated, and different types of fast optical modulators have been applied [13,14].

#### **2.2 Grating Coupler**

Grating can be formed through using periodic, varying structures on a specific surface. Etching on SOI or depositing amorphous silicon on SOI can result in grating and when wavelength of light is smaller than the period of index variation then diffraction occurs. [15-17].

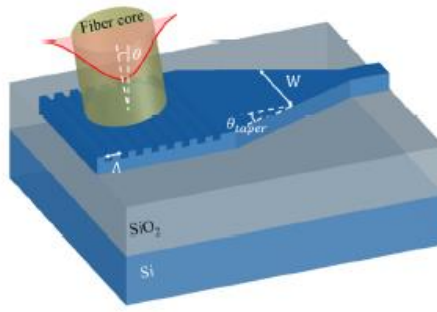


**Figure 2.1:** Schematic structure for a 1D grating coupler (GC) with linear waveguide taper and key parameters: period  $\Lambda$ , fiber tilt angle  $\theta$ , varying taper width  $W$  and taper angle  $\theta_{taper}$ . [18]

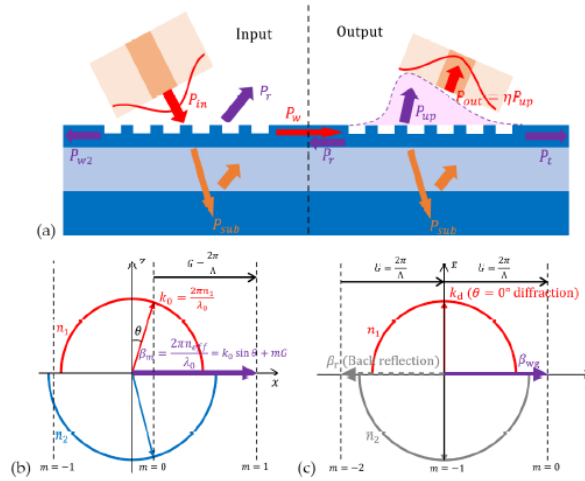


**Figure 2.2:** (a) Loss channels in input and output coupling; (b) wave-vector diagram for fiber-to-chip coupling; and (c) wave-vector diagram for chip-to-fiber perfectly vertical coupling, [18]

In figure 2.2 a, some reasons for power loss or efficiency loss for grating coupler have been illustrated. Firstly,  $P_{sub}$  denotes the power leakage through the substrate which can be minimized if proper oxide thickness is used. Secondly,  $P_r$  stands for the reflected light that also causes a decrease in efficiency. Finally, in the opposite direction of waveguide, some

power is coupled which can be named  $P_{w2}$ . In case of perfectly vertical coupling ( $\theta = 0$ ), there is a strong backward reflection  $\beta_r$  (Figure 2.2c), which reduces the coupling efficiency significantly. [18]

Tapered waveguide can be used to do transition of light to single-mode waveguide and when only dimension of the propagating mode is changed while conserving the energy then it is called adiabatic transition. For adiabatic transition, the linear waveguide must satisfy the following equation,

$$\theta_{taper} < \frac{\lambda}{2Wn_{eff}} \quad (2.1)$$

Where,  $\theta_{taper}$  denotes taper angle, W is waveguide width, modal which is varying,  $n_{eff}$  is the corresponding mode effective index. As shown in figure 2.2(b), modal mismatch between fiber mode and grating profile causes significant losses. Apodized grating coupler provides better efficiency than the uniform one as the coupling strength can be varied along x-direction for the apodized one. [18]

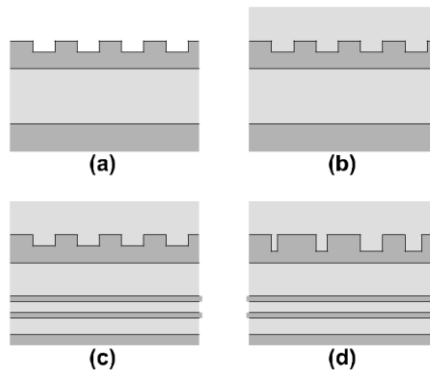


**Figure 2.3:** (a) Schematic drawing of different types of couplers: Uniform grating in (a) SOI with air top cladding, (b) SOI with oxide top cladding, (c) SOI with bottom Si/SiO<sub>2</sub> mirror. In (d), a grating coupler with varying groove widths is shown. Dark gray represents Si and light gray SiO<sub>2</sub>. [19]

Several techniques have been used to improve coupling efficiency. Through using top cladding layer on the Silicon (figure 2.3 (a) & 2.3(b)), the efficiency can be increased where index-matching layer is preferable. Furthermore, two-pair of Si/SiO<sub>2</sub> mirror (figure 2.3 (c)) which acts as a bottom reflector can also be implemented to make the efficiency significantly higher. An optimized non-uniform grating in addition to this reflector (figure 2.3 (d)) can provide better coupling efficiency. [19]

**Table 2.1:** Performance comparison of some exemplary grating couplers

	Wavelength	Polarization	Insertion loss	Bandwidth	Process
2011 [57]	1310nm	TE	-3dB	58nm	400nm Si, Shallow etch
2012 [58]	1550nm	TE	-4.4dB	45nm(1.5dB)	220nm Si, 2nm BOX, shallow etch
2012 [59]	1490nm	TE	-0.75dB	N/A	shallow etch, Bottom DBR
2012 [60]	1550nm	TE	-2.29dB	60nm	full etch, 250 Si, 1 $\mu$ m BOX

### 2.3 Waveguide-to-fiber Coupler fabricated through DLW method

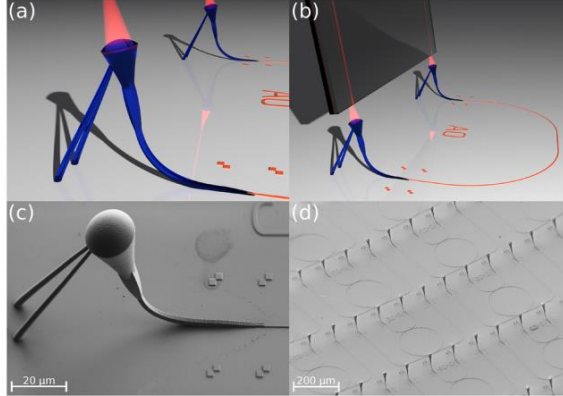


**Figure 2.4:** (a) Rendering of a polymer coupler (blue) attached to a silicon nitride waveguide (orange). The double-square-markers used for alignment are also shown. (b) Rendering of the hybrid photonic circuit for carrying out transmission tests. A fiber array with a pitch of 250 m is placed over the couplers. Both couplers are connected by a silicon nitride single mode waveguide. (c) SEM-micrograph of a fabricated coupler realized by DLW. (d) SEM-micrograph of a photonic chip with several devices illustrating scalable fabrication of hybrid 3D-planar photonic circuits.[20]

The Direct laser writing (DLW) method has been used to fabricate polymer couplers and the dimension of this waveguide can be changed easily. Furthermore, lenses are used at the end of this waveguide which helps to shape the beam and through changing the lenses' curvature the couplers can be tuned for different wavelengths. [20].

### 2.4 Optical Packaging

Optical Packaging can be implemented to design integrated silicon-photonics based transceiver where Tx and Rx components, laser, micro-optics, control-optics are all embedded on a single silicon photonic chip. Instead of bonding optical fiber to chip, the idea of pluggable connection of fiber has been introduced here through micro-optics which

opens the door for packaging setup without degrading the performance of both transmitter and receiver. [31]

The compatibility between photonic subsystem (that is compact and integrated) and CMOS (complementary metal–oxide–semiconductor) technology acts as the building blocks for Silicon photonics. This field has also been made more diversified through the application of new materials instead of only silicon for example, SOI [ 32,33], Ge [34], InP [35] , Si<sub>3</sub>N<sub>4</sub> [36] to name a few. As a result, optical (active) elements can be embedded in a more efficient way.

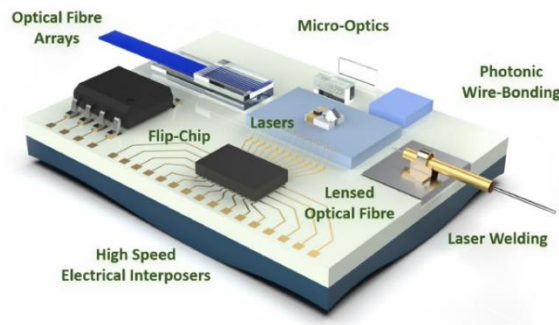


**Figure 2.5:** Various packaging technologies available through PIXAPP.

Different types of photonic elements for example 1D and 2D grating couplers, edge couplers, splitters, integrated lasers, arrayed waveguide gratings (AWG), multiplexers/de-multiplexers, thermally tunable microring resonators, high-speed Ge photodiodes, thermo-optic phase shifters, electro-absorption modulators (EAMs), etc. can be fabricated on a single wafer and through customizing the design and elements, a wide variety of PIC design is possible to make. It reduces the cost and makes the production more feasible as it does not require to make single wafer for each element. Furthermore, through interfacing

between electrical and optical elements a desired output can be obtained from a very small chip. Now the goal is to have a connection between PIC and its surroundings. [31]

An optically and electrically interfaced PIC has been shown in figure 2.5. Photonic packages comprise of electrical, optical, mechanical, and thermal core. [37] For alignment, special care needs to be taken otherwise it may lead to a significant optical loss [38-42].

The optical and electrical elements can be implemented on PIC through 3 different processes or strands. (Fig 2.6)

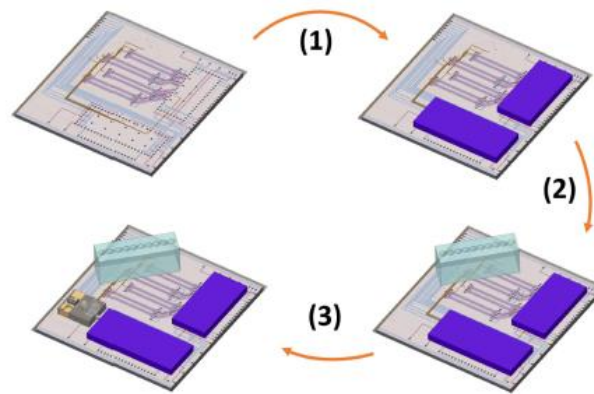


**Figure 2.6:** Schematic of packaging the first 3 assembly strands on PIC. The (1) deals with EICs, (2) with microlenses, and (3) with the MOB.

The first strand is Electronic integrated circuit (EIC) integration. A driver for Mach Zehnder Modulators (MZMs) and Trans Impedance Amplifier (TIA), work as 2 EIC in transmitter and receiver side respectively for each PIC. (Fig 2.6).

The second strand is Microlenses. In figure 2.6, the PIC comprises 8 grating couplers which couples light to the PIC at  $10^\circ$  coupling angle, while having similar Mode field diameter of ( $9.2 \mu\text{m}$ ) SMF28 fiber at 1310nm wavelength. On top of the Fiber array and PIC, the

Microlenses were placed which couples light from PIC to a certain distance through collimating the diverging beam. Furthermore, Microlenses serve the purpose of increasing the MFD. Consequently, the optical loss is due to misalignment is minimized significantly resulting in good performance of optical data-link [31]

Micro-optical bench (MOB) is very small in size and so it can be placed anywhere on the PIC. The MOB is comprised of Laser on a substrate. A ball lens focuses its (laser) output. This focused beam then reflected by prism by  $10^\circ$  angle to couple with a grating coupler. (Figure 2.7) [31]

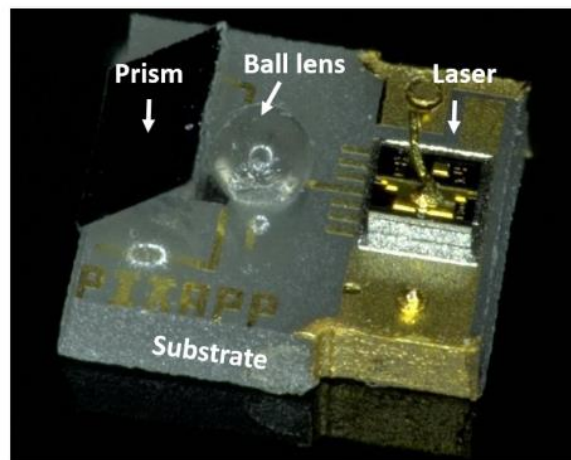


*Figure 2.7: MOB setup connected with ball lens and prism.*

A proper design of MOB can decrease the output power of laser while maintaining enough dissipation of heat. After the completion of the 3 strands (EIC, Microlenses and MOB), an integrated PIC component is formed.

### **2.5 Precision micro-dispensing Process**

Precision microdispensing offers state of the art technology with remarkable volumetric control (100 Picolitre) and dots scales down to  $50 \mu\text{m}$  which differs from material to

material while maintaining spectacular speed of 5dots/sec. This process has been implemented successfully in 3D Manufacturing, Microelectronics Packaging, Printed Electronics, Biomanufacturing to name a few.[43]

The adhesive force between the work piece and liquid plays a vital role for dispensing a drop after making close contact between liquid and work piece. High accuracy can be achieved through piezoelectric actuator while the process of dispensing the liquid on workpiece is controlled by PID (Proportional – Integral – Derivative) controller. [44]

Three main techniques can be implemented in microdispensing process, first one is time pressure where amount of dispensed liquid is proportional to the pressure applied, second one is rotary screw or continuous approach where motor-driven screw is used for the continuous motion of the dispensing liquid. The third one is piston-like approach piston-like structure is used for dispensing and this could be continuous or discontinuous.

The dimension of droplet can be varied only by changing the injector or nozzle while controlling with the same piezoelectric actuator system. As a result, accuracy and cost can both be optimized.

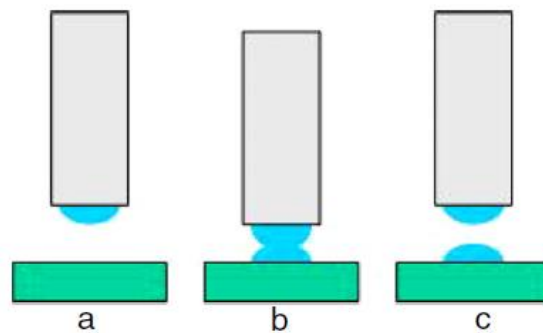


**Figure 2.8:** Sequential process of the making of droplet (a) (a) Preparatory position (no droplet created), (b) Dispensing position (droplet in-progress), (c) Returning position (droplet created). [44]

In figure 2.8, droplet formation technique has been depicted where surrounding medium moves, and liquid displacement takes place. Four types of forces are experienced by the liquid at rest namely gravitational force  $F_g$ , pressure force  $F_p$ , surface tension force  $F_\sigma$ , viscous force  $F_\mu$ .(Figure 2.9)



**Figure 2.9:** Force analysis of the droplet at the tip of the injector. [44]

Meniscus experiences gravitational force when its mass is affected by gravity. Pressure on top of the liquid gives rise to pressure force. When there is an unbalance of molecular force at the interface of liquid and air, surface tension force takes place. Finally, liquid viscosity is responsible for viscous force. In microdispensing system, it is assumed that piezo-actuator displacement controls the diameter of the droplet.

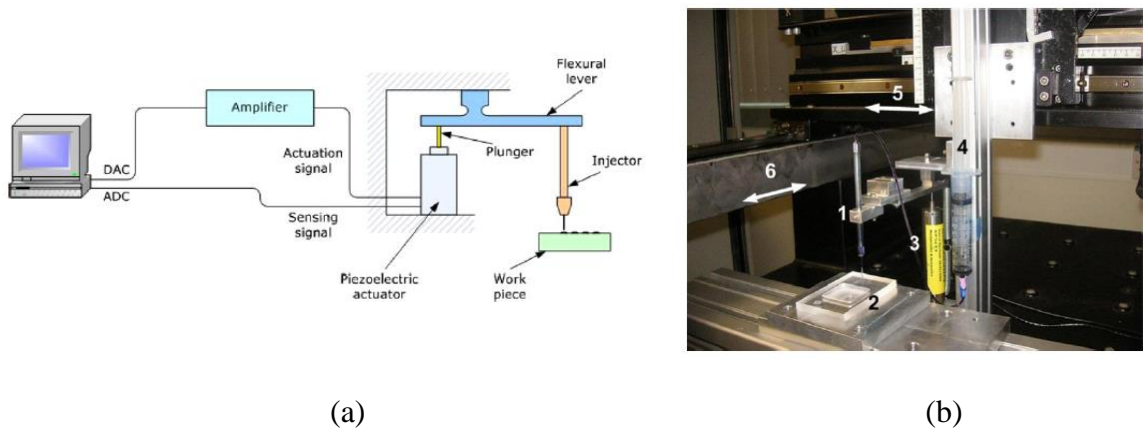


**Figure 2.10:** (a) Complete installation of microdispensing system (b) Microdispensing installation in X\_Y table; (1) injector, (2) workpiece, (3) piezoelectric actuator, (4) liquid container, (5) X-axis, (6) Y-axis. [44]

In figure, 2.10(b), experimental setup has been illustrated where microdispensing system is connected to X-Y table so that different patterns or designs can be generated through following trajectories. Three PID controllers (each for X-axis, Yaxis and Z-axis/piezoelectric actuator) control the trajectory and droplet uniformity. Control systems also include computer control, Analogue to digital converter (ADC), Digital to Analogue (DAC) converter and amplifier. The whole schematic of microdispensing system is depicted in Figure 2.10(a).

## 2.6 Micro-lens array through ink-jet printing

Micro-lens and micro-lens array (MLA) can be implemented to numerous applications such as light emitting devices [45-47], sensors [48], fiber-coupling devices [49], vertical cavity surface emitting lasers (VCSEL) [50] and so on. MLA applications require high-NA to maintain a good quality of the image.

MLA can be fabricated through ink-jet printing method where dimension of the lens and optical characteristics can be optimized. Larger field-of-view and remarkable sensing can also be realized through implementing MLA on a curved surface. [51]

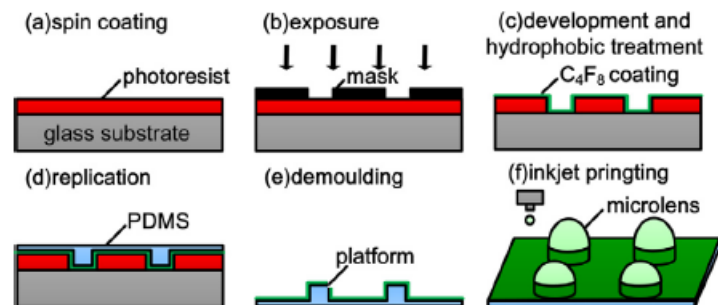


**Figure 2.11:** (a–e) Illustrative steps of the micro platforms fabrication process; (f) MLA inkjet printing process.

Micro-platform preparation and ink-jetting of polymer are the two main processes for the fabrication of MLA having high NA (Figure 2.11). In figure 2.11 (a) and (b), photolithography technique is used to make holes of circular shape. Then C<sub>4</sub>F<sub>8</sub> treatment accelerates the demolding process (figure 2.11(c)). PDMS precursor is poured on the hole to fill them, and heat is given for a certain amount of time to have solid PDMS (figure 2.11(d)). After that, micro-platform with PDMS substrate is separated (figure 2.11 (e)). In the final stage, micro-lens array is ink-jetted on the micro-round platform. (Figure 2.11(f)). [51]

## 2.7 Far-field Projection

According to the Fresnel diffraction theory, from the near electric field distribution far electric field distribution can be found [21,22]

$$e(x_1, y_1) = \frac{j \exp(-jkz_0)}{\lambda z_0} \exp\left(-\frac{jk}{2z_0}(x_1^2 + y_1^2)\right) \iint e(x_0, y_0) \exp\left(-\frac{jk}{2z_0}(x_0^2 + y_0^2)\right) \exp\left(\frac{j2\pi}{\lambda z_0}(x_0 x_1 + y_0 y_1)\right) dx_0 dy_0 \quad (2.2)$$

$e(x_0, y_0)$  corresponds to near electric scalar field in  $x_0 y_0$ -plane whereas  $e(x_1, y_1)$  provides the information about far electric scalar field in  $x_1 y_1$ -plane. Free space wave vector is denoted by  $k$ .

Far-field radiation pattern can be written as,

$$e(x_1, y_1) = F(\theta_x, \theta_y) \frac{\exp(jkR)}{R} \quad (2.3)$$

Where  $\theta_x$  and  $\theta_y$  means lateral and longitudinal beam steering angle respectively.

In case of  $M \times N$  OPA having lateral and longitudinal pitch of  $\delta_x$  and  $\delta_y$  respectively, the far field can be written as

$$e(x_1, y_1) = \sum_{m=0}^{M-1} \sum_{n=0}^{N-1} A_{mn} \cdot F_{mn}(\theta_x, \theta_y) \frac{\exp(jkR)}{R} \cdot \exp\{-jk(m \cdot \delta_x \sin \theta_x - \beta_{mx})\} \cdot \exp\{-jk(n \cdot \delta_y \sin \theta_y - \beta_{ny})\} \quad (2.4)$$

Where  $A_{mn}$  denotes field amplitude,  $F_{mn}(\theta_x, \theta_y)$  is the radiation patterns of antenna

located at different position,  $R_{mn} = \sqrt{(x_1 - m\delta_x)^2 + (y_1 - n\delta_y)^2 + z_0^2}$  ;  $\beta_{mx} = \frac{m\Delta\phi_x}{k}$ ,  $\beta_{ny} = \frac{n\Delta\phi_y}{k}$  are the phase differences.

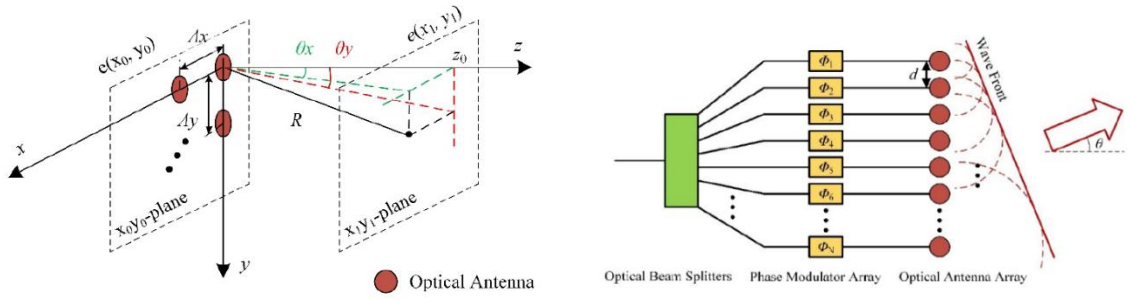


**Figure 2.12:** (a) Schematic of a 2D OPA (b) Operational principle of phased array [22]

Through normalizing equation (2.4), array factor  $T(\theta_x, \theta_y)$ , can be written as,

$$T(\theta_x, \theta_y) = \frac{\sin\left[\frac{M}{2}(k\delta_x \sin \theta_x - \Delta\phi_x)\right]}{M \sin\left[\frac{1}{2}(k\delta_x \sin \theta_x - \Delta\phi_x)\right]} \cdot \frac{\sin\left[\frac{N}{2}(k\delta_y \sin \theta_y - \Delta\phi_y)\right]}{N \sin\left[\frac{1}{2}(k\delta_y \sin \theta_y - \Delta\phi_y)\right]} \quad (2.5)$$

The main components of OPA are optical beam splitters, a phase modulator array, and an optical antenna array (figure 2.5b). The power that comes from the laser is distributed through the beam splitters to the phase modulator array and optical antenna array. Grating couplers can be used as emitters or optical antenna array. Phase modulator

array controls the optical wavefront and hence steers the far-field beam. From equation 2.5, the normalized array factor will be higher when the following equation is satisfied,

$$\frac{k\delta \sin \theta - \Delta\phi}{2} = p\pi \quad (2.6)$$

here,  $p = (\dots \dots \dots, -3, -2, -1, 0, 1, 2, 3, \dots \dots \dots)$ .

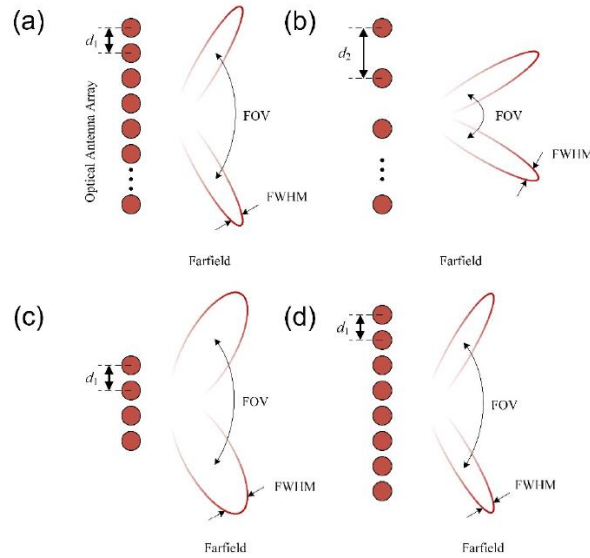


**Figure 2.13:** Schematic diagram of far field beam with different spacing and aperture condition.[22]

With the increase of absolute value of P, the phase difference between two adjacent antennas also increases and therefore more power is consumed though phase modulator. Consider that the central principal maximum, the relationship between the phase difference of the adjacent phase unit  $\Delta\phi$ , and the beam steering angle  $\theta$  are shown in the following equation,

$$\theta = \sin^{-1} \left( \frac{\Delta\phi \cdot \lambda}{2\pi \cdot d} \right) \quad (2.7)$$

where  $\lambda$  is the wavelength and d is the interval of antennas, as shown in Figure 2.5b.

As shown in Figure 2.6a, when  $\Delta\Phi = \pi$ , the central principal maximum is located at  $\sin^{-1}(\lambda/2d)$  and the -1th order lobe is at  $-\sin^{-1}(\lambda/2d)$ . The FOV is given by:

$$\Delta\theta_{\text{FOV}} = \sin^{-1}\left(\frac{\lambda}{2d}\right) \quad (2.8)$$

When  $Nd \gg \lambda$ , the full width at half maximum (FWHM) is given by:

$$\Delta\theta_{\text{FWHM}} \approx \frac{0.866\lambda}{Nd \cdot \cos\theta} \quad (2.9)$$

According to equation (2.8) and (2.9), FOV and FWHM both depend on the aperture size and different intervals. From figure 2.6a, b, it is obvious that when the optical antenna array is densely spaced, they provide larger FOV than the widely spaced one. Furthermore, from figure 2.6 c, d, it can be said that narrower beam width or higher resolution can be achieved when aperture size is larger while maintaining same  $d$  (interval of antennas). [22].

## Chapter 3

### OPTICAL PACKAGING THROUGH GRATING COUPLER

#### 3.1 Design principle of Grating Coupler

In the Grating coupler design structure (Figure 3.1), Si substrate is used with thickness 1 $\mu$ m. On top it there is SiO<sub>2</sub> having thickness of 3 $\mu$ m. The apodized grating coupler with waveguide that corresponds to device layer, is made of Silicon with thickness 0.25 $\mu$ m and have been built on the buried oxide layer. The designed patterns, for example waveguides, gratings were fabricated through defining positive resist, then resist development and finally dry-etching processes. Plasma-enhanced chemical vapor deposition (PECVD) is used to deposit very thin (< 20nm) SiO<sub>2</sub> layer for protection on the device layer. [56]

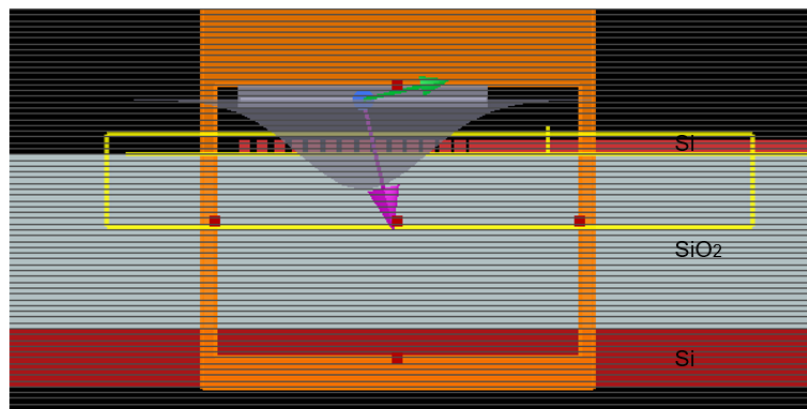


*Figure 3.1: Grating coupler on SOI substrate*

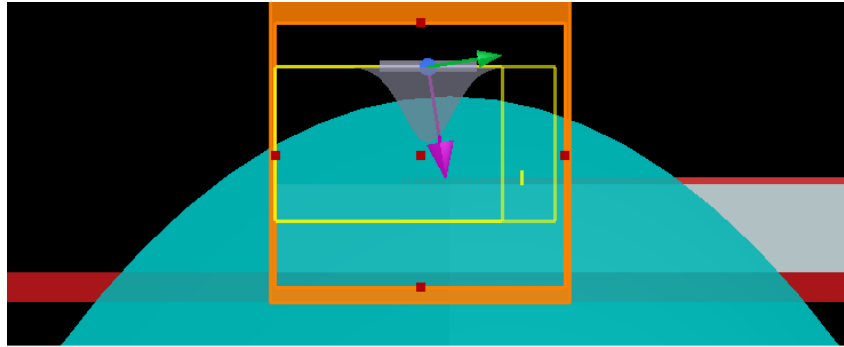


**Figure 3.2:** Hemi-spherical lens on grating coupler

### 3.2 Micro-dispenser-based lens printing on grating coupler

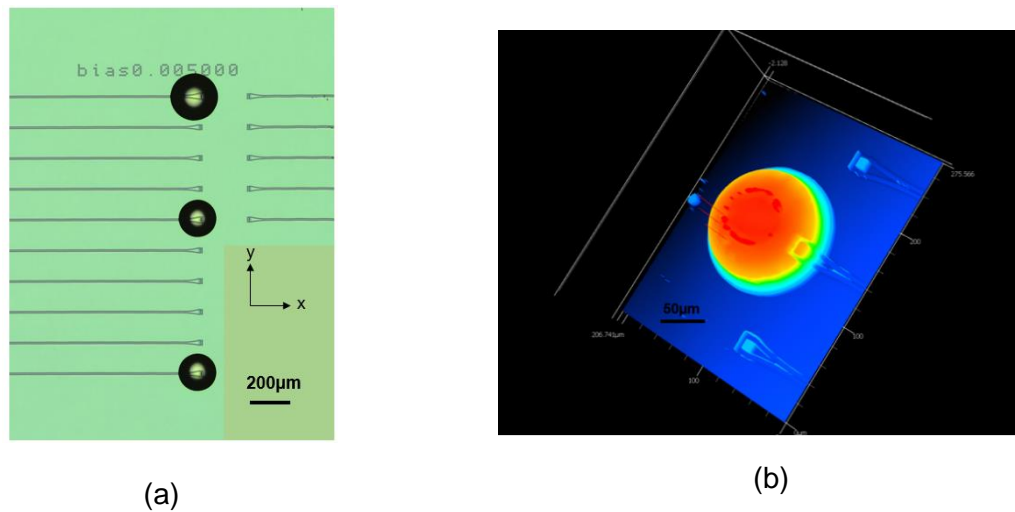


**Figure 3.3:**(a) Top view of micro-lens printed on grating coupler captured by camera in microdispensing system. (b) Perspective view of the lens on grating coupler captured by confocal laser microscope system. [53]

Micro-dispenser based additive manufacturing approach was taken to print the index-matched ( $\mu=1.55$ ) UV epoxy made  $\mu$ lenses on the grating coupler. The lenses are of hemi-spherical shape. (Figure 3.3). Subnanoliter volumetric control can be realized through the nScript 3Dn-300 for the adhesive which is UV curable. The diameter of the  $\mu$ lenses depend

on nozzle diameter. In this work, nozzle diameter of 25  $\mu\text{m}$  was implemented to have certain diameter range (50 $\mu\text{m}$  -150  $\mu\text{m}$ ). Open duration of the valve system (0.01-0.05s) was also maintained for control. The adhesive was then laid down while the valve in the microdispensing tool was opened for 0.5 seconds, operated by a print command. On the print bed, rapid solidification was performed on the microdispensed lens array through using UV flashlight ( $\lambda=365\text{nm}$  at 15W) for 1 minute. In this way, the formation of the  $\mu\text{lens}$  array can be preserved. Finally, the sample was put on the UV chamber for further cure ( $\lambda=365\text{nm}$  at 93mW/cm<sup>2</sup>) after removing form the print bed.[53]

### 3.3 Microlens dimension calculations through Profilometer

A profilometer has been used to measure the profile of the hemispherical lens structure. Several exemplary lenses were tested under the Keyence VK-X3000 3D surface profiler to calculate the in-plane radius  $r$  and height  $h$  for each microlenses.

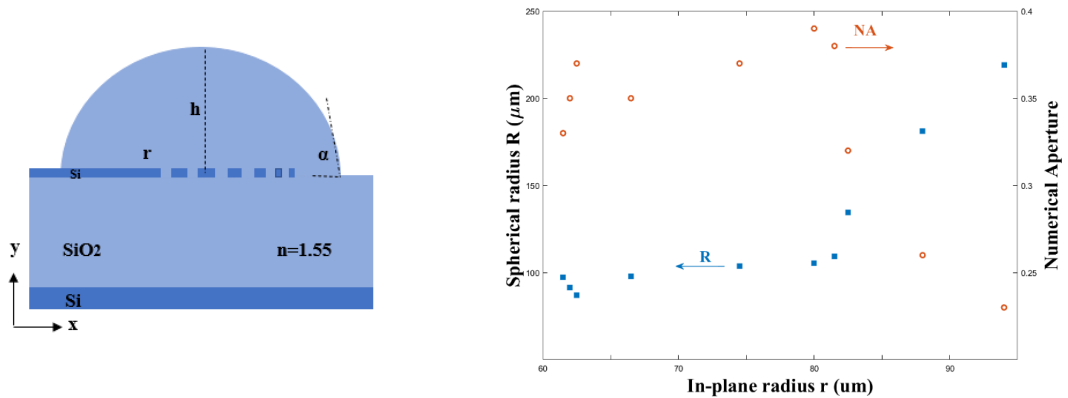


**Figure 3.4:**(a) Schematic diagram of the devices' cross-section. The contact angle ( $\alpha$ ) on the interface determines the numerical aperture of the lens. (b) Measured spherical radius  $R$  and versus in-plane radius  $r$  measured across the 10 micro-lenses produced by the dispenser. Right y-axis: correspondent numerical radius.

The height( $h$ ) and in-plane radius ( $r$ ) have been measured. The spherical radius can be found from:  $R = \frac{h}{2} + \frac{r^2}{2h}$ . As we know the refractive index ( $n$ ) of the UV epoxy ( $n=1.55$ ) and also from the calculated  $R$ , the focal length ( $f$ ) and  $NA$  can be estimated from the following equations.

$$f = \frac{R}{n-1} \quad (3.1)$$

$$\text{and } NA = \frac{1}{\sqrt{1+(\frac{f}{r})^2}}; [\text{here, } \frac{f}{r} = \frac{1}{2(n-1)}(\frac{h}{r} + \frac{r}{h})] \quad (3.2)$$

The interaction at the interface and the polymer's viscosity determines the contact angle between the UV polymer and the SOI substrate.

$$r = R \sin \alpha \quad [1] \quad (3.3)$$

We are able to derive: after substituting  $R$  for the expression versus  $h$  and  $r$ ,

$$\frac{2}{\sin \alpha} = \frac{h}{r} + \frac{r}{h} \quad (3.4)$$

After substituting this factor into the expression for  $NA$ , we can obtain:

$$NA = \frac{1}{\sqrt{1+(\frac{1}{\sin \alpha(n-1)})^2}} \quad (3.5)$$

According to Equation 3.5, the  $NA$  ought to be independent of the droplet size  $r$ . Multiple droplets are used to demonstrate experimentally the independence of the  $NA$  and  $r$  (Fig. 3.4b). The  $NA$  stays around 0.36 for droplets with an in plane radius  $r$  of less than  $80 \mu\text{m}$  (orange circles in Fig.3.4b), also at this  $NA$ , the spherical radius  $R$  remains around  $100 \mu\text{m}$  (blue squares in Fig. 3.4b). The numerical prediction in equation (3.5), where the contact angle  $\alpha$  is calculated to be 0.78 rad on the glass surface (Fig.3.4b), is consistent with the size-independent  $NA$ .  $NA$  decreases because of larger droplets. Using an optical microscope,  $r$  can be calculated quickly to estimate the  $NA$  of newly prepared droplets.

### 3.4 Experimental Analysis

#### 3.4.1 Coupling for incoming beam

We used TE polarized Gaussian beam as source in the simulation region where the wavelength ranges from 1.3um to 1.6 um which refers to the optical communication band.

The incident angle has been varied from  $0^\circ$  to  $40^\circ$  through parameter sweep.

A hemisphere with spherical radius  $R=100\mu\text{m}$  and  $150\mu\text{m}$  has been used as lenslet on top of the grating coupler (Figure 3.2). The refractive index of the sphere is 1.55 which is similar to the refractive index of UV epoxy. Additionally, this lens is indexed matched with the SOI substrate which may lead to better light confinement.

In this case, the same gaussian source has been used while keeping the same wavelength range (1.3-1.6um).

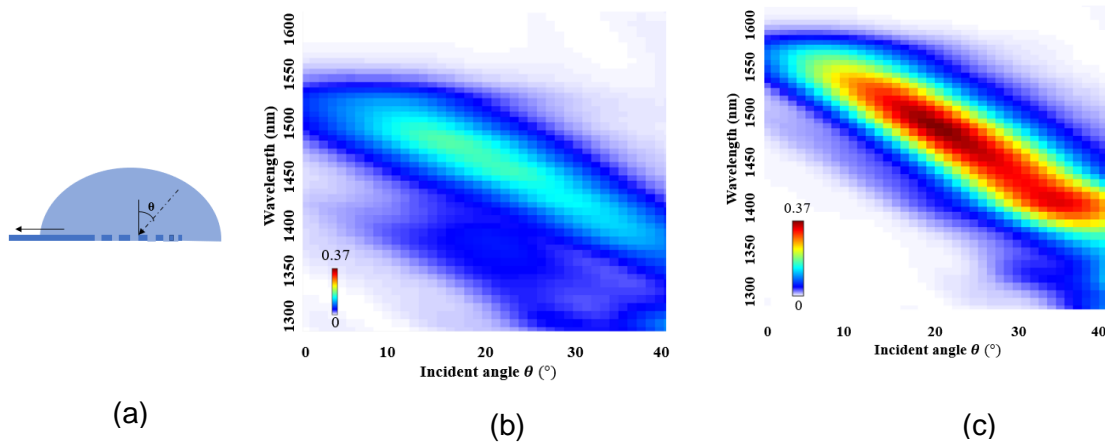


**Figure 3.5:**  $\mu$ lens modified fiber-chip coupling spectra. (a) Cross-sectional schematics indicating the incident angle  $\theta$ . (b) Transmission spectra versus incident angle for the apodized grating coupler defined on SOI and (c) same device with  $\mu$ lens

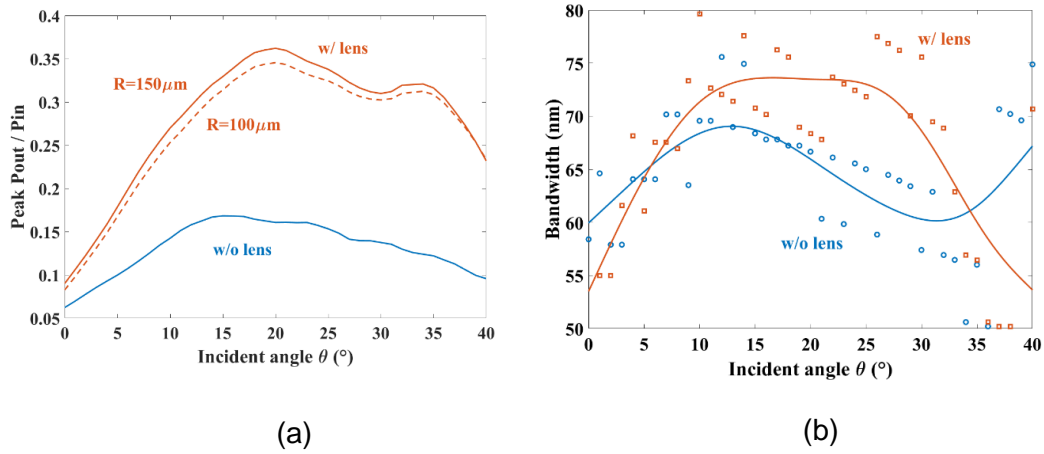


**Figure 3.6:** (a) Peak transmission versus incident angle at the optimal transmission wavelength in b and c for without (blue) and with  $\mu$ lens (orange). (b) The extracted full-width half maximum bandwidth of transmission spectra versus incident angle for both conditions.

Further parametric sweep varying incident angle from  $0^\circ$  to  $40^\circ$  have been performed. The transmission for grating coupler with and without lens has been compared for this different incident angles (Figure 3.6b)

It is observed that for the grating coupler structure without lens, the peak transmission is 15% at the incident angle of  $15^\circ$  whereas after adding lens we obtain the peak efficiency at around 35% for the incident angle of  $20^\circ$  (Figure 3.6 (a))

Also, it is important to note that 20% increase in transmission is significantly attributed to the  $h$  adjustment. Additionally, from the 2d plot it is certain that transmission intensity is higher for with lens structure than the bare grating structure (Figure 3.5b and 3.5c). Bandwidth has also been increased by 10-20 nm in between the incident angle  $10^\circ$  to  $30^\circ$  when lens has been introduced (Figure 3.6b).

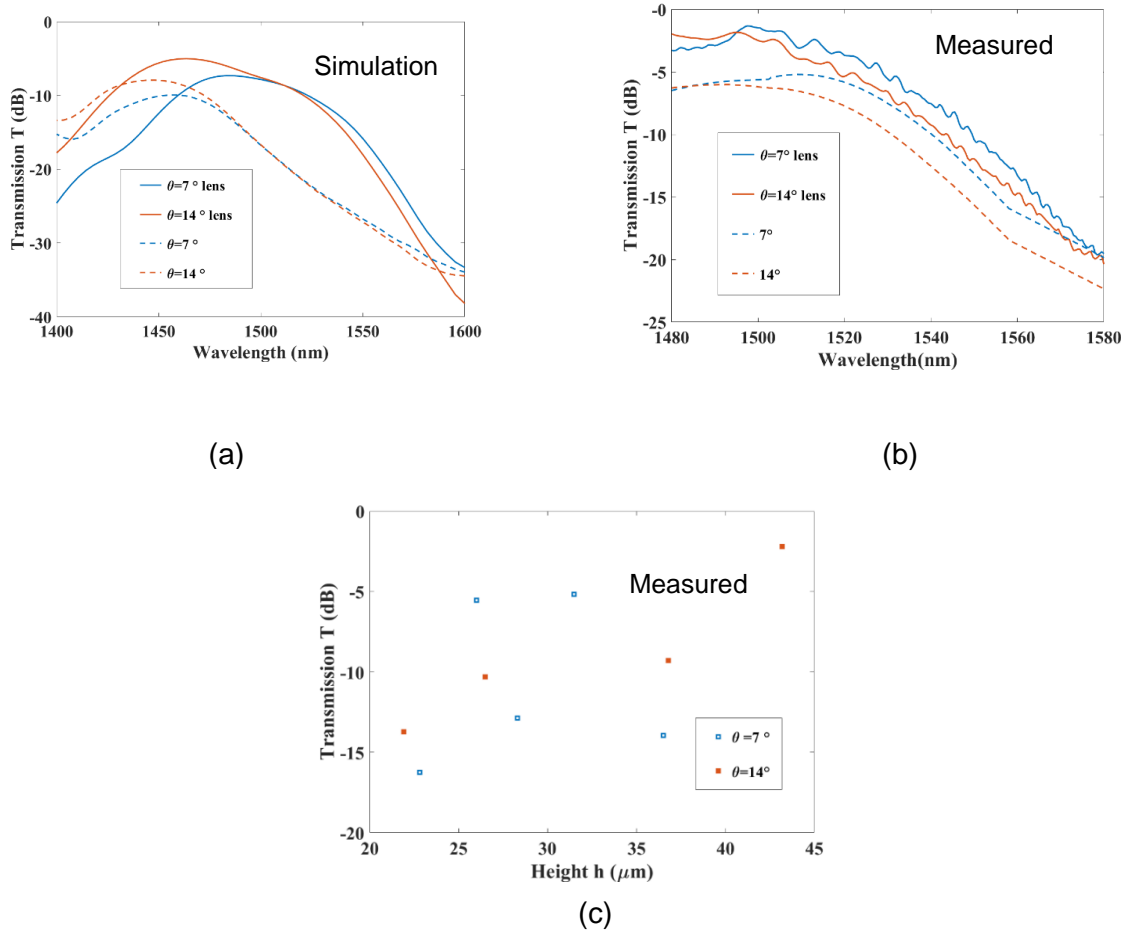


**Figure 3.7:** Measured optical characteristics. (a) Numerically predicted and (b) measured transmission spectra of the  $\mu$ lens atop grating coupler with (orange) and the same design without  $\mu$ lens (blue), at the incident angles of  $7^\circ$  (dashed) and  $14^\circ$  (solid curves). (c) Peak transmission of  $\mu$ lens atop grating couplers versus the height of the  $\mu$ lens for the incident angle of  $7^\circ$  (blue) and  $14^\circ$  (orange).

In the FDTD simulation, for two incident angles (  $7^\circ$  and  $14^\circ$  ) we compared transmission spectra for with and without lenses (figure 3.7(a)). In case of without lenses, both the incident angles showed almost same peak (-11 dB at  $7^\circ$  and -9dB at  $14^\circ$  respectively) and same pattern of changes along the different wavelengths. Additionally, for with lens structure, at  $7^\circ$  incident angle the peak is at -9dB whereas for  $14^\circ$  , there is an improvement of transmission around -3dB. The transmission spectra also follows almost the same pattern of changes. In the experiment, angle controller (Thorlabs Nanomax 300) has been used which can tune the incident angle of single mode fiber between  $5^\circ$ - $15^\circ$ .

A tunable laser has been used as a source to the chip through the polarization controller. The output light from the grating coupler is collected by another single mode fiber and a power meter connected to it gives the value of the output power. It is observed that in case of without lens both the  $7^\circ$  and  $14^\circ$  has showed almost same transmission at around -6db for the wavelength of 1480nm (Figure 3.7b)

Significantly higher transmission is noticeable after lenses have been placed on the grating coupler structures through micro dispensing. Peak transmission of around -2.5dB is spotted for both  $7^\circ$  and  $14^\circ$  incident angles. In this experiment, 11 microlenses have been placed on the grating coupler and they are compared with another bare corresponding 11 grating coupler structure.

Transmission and height are proportional to each other (Figure 3.7 (c)). Some discrepancies are also observed due to misalignment and fabrication variation.

### 3.4.2 Coupling for outgoing beam (Far-field projection)

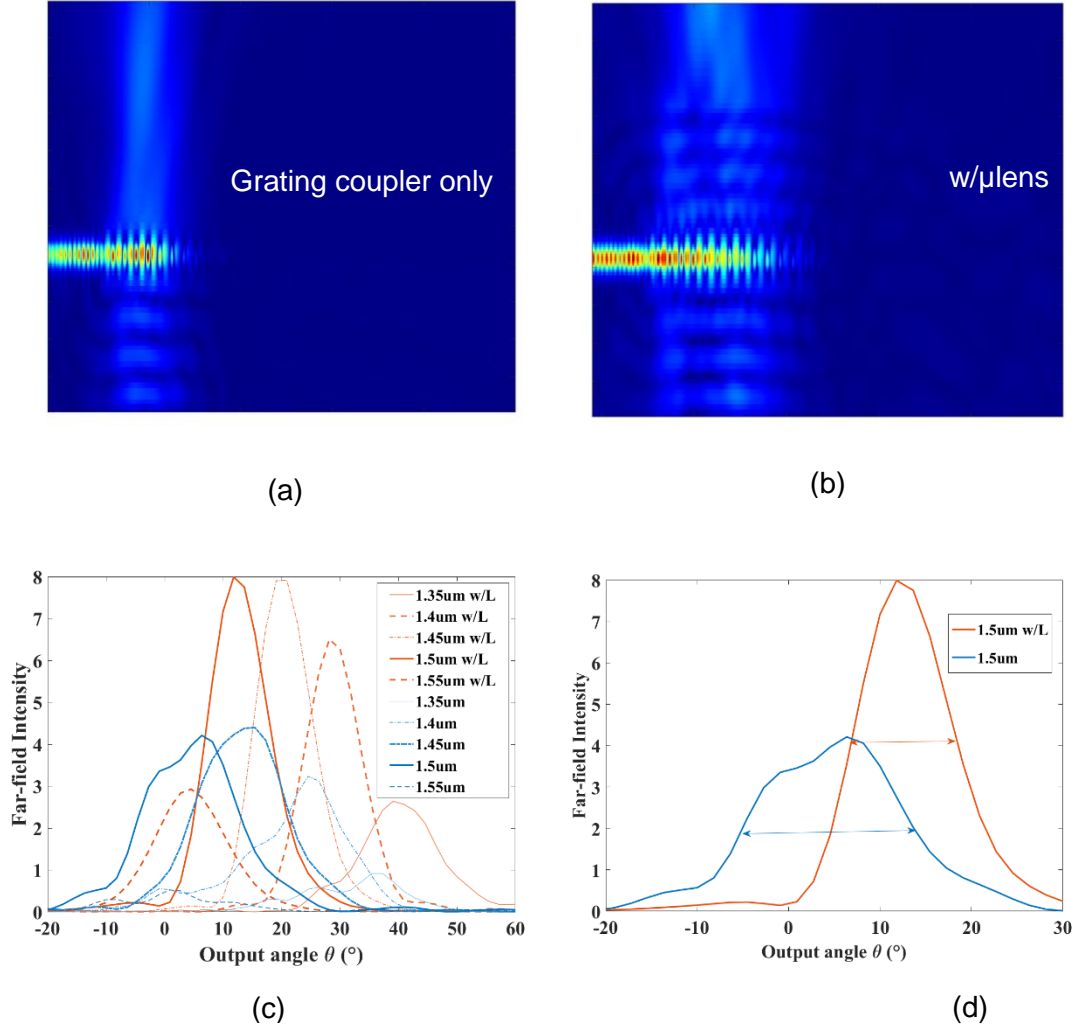


**Figure 3.8:**  $\mu$ lens modified far field projection for dispersion-based beam steering. (a) Cross-sectional view of the grating coupler with in-waveguide excitations, and (b) after adding the  $\mu$ lens ( $R=100 \mu\text{m}$ ,  $h=2.75\mu\text{m}$ ). (c) Incident wavelength-dependent far-field projection, for bare grating coupler (blue) and with  $\mu$ lens (yellow). (d) Selective far field project at the input laser wavelength of  $1.50 \mu\text{m}$  (at the distance of  $1\text{m}$ ).

Grating couplers can be used as emitters in near and far-fields which has been investigated in (figure 3.8). When mode source (as in-waveguide excitation) has been used the cross-sectional view has been compared before (fig.3.8a) and after adding the  $\mu$ lens (Fig. 3.8b).

The optical field is restricted to the first half of the grating coupler ( $10\ \mu\text{m}$ ) without the top cladding layer. The peak angle can range from 0 to 40 degrees, depending on the wavelength of the input laser. As an alternative method to fiber-chip coupling (Fig. 3.5a and 3.6 a), and the far field peak transmission also goes up with lens cladding (the orange curves in Fig. 3.8c) for different wavelengths.

The surface of the curve contributes to the reduction of angular spreading, (figure 3.8 b) resulting in a smaller spot-size in the distant field. It is anticipated that the angular spreading will be reduced by nearly 50% at an incident wavelength of  $1.5\ \mu\text{m}$  (Fig.3.8d).

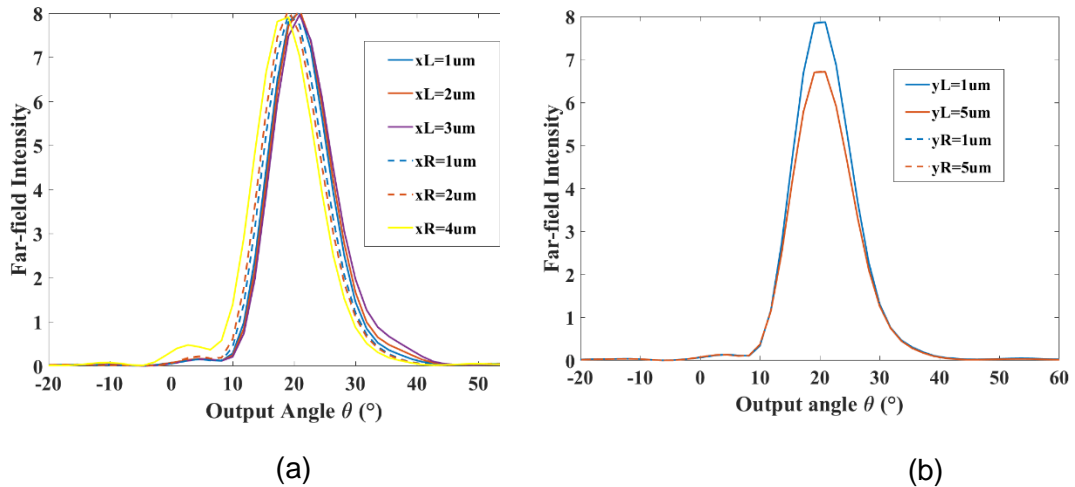


**Figure 3.9:** Incident wavelength-dependent far-field projection, (a) misalignment in the x-direction, and (b) y direction after adding the  $\mu$ lens ( $R=100\ \mu\text{m}$ ,  $h=2.75\ \mu\text{m}$ ).

The misalignment between  $\mu$ lens center and grating coupler center has also been considered in Figure 3.9. For the wavelength of  $1.4\mu\text{m}$ , we considered misalignment for both x and y direction. As for x-direction, small misalignment (at left and at right) does not cause significant change in the transmission spectra while a small shift of the pattern is observed for different misalignments. (Figure 3.9 (a)).

When misalignment in the y-axis is considered (Figure 3.9b), we observed that for misalignment (at left and at right) of  $1\mu\text{m}$  transmission remains same as the ideal case (Figure 3.8 (c)) where there is no misalignment. But if misalignment increases to  $5\mu\text{m}$  in both right and left side, the intensity decreases. For the same misalignment, the intensity does not depend on direction (i.e.,  $1\mu\text{m}$  misalignment whether left or right, gives the same intensity). So, certain symmetry is observed here. Note that the FWHM has not changed for both x and y misalignment and it can be said that the resolution is not affected by the misalignment.

## Chapter 4

### CONCLUSIONS AND PERSPECTIVES

The goal of this study is to combine microdispensing process with integrated photonics and develop novel packaging systems to perform optical coupling for different applications. With the collaboration with other researchers, the author was able to go through the whole process of design, simulation, fabrication, and experiments.

First, the author proposed micro-lens printed on the vertical coupler through microdispensing process and this technique requires less complexity with high efficiency. Furthermore, this technique requires less time to print on a large array of grating couplers in compare to other additive manufacturing processes. High NA can be achieved which helps to increase the angle tolerance for the input fiber.

The property of outgoing beam in far-field projection has also been investigated. The shape of the micro-lens has a profound effect on reducing angular spread of the output beam to have better resolution and imaging quality.

Based on the proposed idea of this work, there are some initiatives that can be taken in future to further improve performance.

**Firstly**, we can use different modes for example here we used single TE modes for simulation and single mode fiber in experiment. Different modes such as TM or even multimode can be used to see the effect.

**Secondly**, tiny metastucture can be designed and carefully placed on top of the microlenses through microdispensing to control the property of incoming and outgoing light more effectively.

**Thirdly**, in this work we were mainly focused on S-band (1460nm-1530nm), C-band(1530nm-1565nm) and L-band(1565nm-1625nm). In today's world, at C-band, the lowest loss can be found for optical fibers whereas L-band is the second lowest in terms of optical losses. Both C-band and L-band can be used in WDM, EDFA technology and so on.[54] Higher chromatic dispersion and lower attenuation per kilometer are the main attributes of the C-band.

On the other hand, O-band (1260-1360 nm) demonstrates higher attenuation per kilometer and very low chromatic dispersion, and this is the first band used for optical communication. [55] O band wavelength scheme can be applied for this work and the optical performance could be increased.

**Fourthly**, for far-field projection, different wavelengths have been used and ring resonator can be used at the output of the far-field projection as an optical filter to have desired wavelength which may help to coupling of light from waveguide to waveguide more efficiently.

This work has proposed and verified a new way to optical packaging having potential application in Sensing, Imaging, LIDER system, free-space communication to name a few. With additional instrumental setup and more advanced strategy, I hope more progress can be achieved.

## REFERENCES

- [1] E. A. Sanchez et al. “Chalcogenide glass microlenses by inkjet printing”. In: *Applied Optics* (2011).
- [2] Riccardo Marchetti et al. “Coupling strategies for silicon photonics integrated chips”. In: *Photonics Research* (2019).
- [3] Y. A. Vlasov et al “ Losses in single-mode silicon-oninsulator strip waveguides and bends”, *Opt. Express* (2004).
- [4] P. Dumon et al “Low-loss SOI photonic wires and ring resonators fabricated with deep UV lithography”, In: *IEEE Photon. Technol. Lett.* (2004).
- [5] R. Marchetti et al “Group-velocity dispersion in SOI-based channel waveguides with reduced-height” In: *Opt. Express* (2017)
- [6] G. F. R. Chen et al “Broadband silicon-on-insulator directional couplers using a combination of straight and curved waveguide sections” In: *Science* (2017)
- [7] Y. Zhang et al “A compact and low loss Y-junction for submicron silicon waveguide” In: *Opt. Express* (2013).
- [8] X. Wang et al “Narrow-band waveguide Bragg gratings on SOI wafers with CMOS-compatible fabrication process” In: *Opt. Express* (2012)
- [9] W. Bogaerts et al “Compact wavelength-selective functions in silicon-on-insulator photonic Wires” In: *IEEE J. Sel. Top. Quantum Electron* (2006)
- [10] C. Lacava et al “ “Integrated nonlinear Mach Zehnder for 40 Gbit/s all-optical switching,” In: *Opt. Express* (2013)
- [11] W. Bogaerts et al “Silicon microring resonators,” In: *Laser Photon. Rev.* (2012)
- [12] R. Marchetti et al “Low-loss micro-resonator filters fabricated in silicon by CMOS-compatible lithographic techniques” In: *Applied Sciences* (2017)
- [13] G. T. Reed et al “Silicon optical modulators” In: *Nat. Photonics* (2010).
- [14] D. J. Thomson et al “50-Gb/s silicon optical modulator,” In: *IEEE Photon. Technol.Lett* (2012).

- [15] Halir et al “Waveguide sub-wavelength structures: A review of principles and applications.” In: *Laser Photonics Rev*(2015)
- [16] Halir et al “. Subwavelength-Grating Metamaterial Structures for Silicon Photonic Devices”. In: *Proc. IEEE* (2018).
- [17] Zhou, W et al “. Subwavelength Engineering in Silicon Photonic Devices” . In : *IEEE J. Sel. Top. Quantum Electron.* (2019).
- [18] Lirong Cheng et al “Grating Couplers on Silicon Photonics: Design Principles, Emerging Trends and Practical Issues” In: *micromachines* (2020)
- [19] Dirk Taillaert et al “Grating Couplers for Coupling between Optical Fibers and Nanophotonic Waveguides” In: *Japanese Journal of Applied Physics* (2006)
- [20] H. Gehring et al “ Low-loss fiber-to-chip couplers with ultrawide optical bandwidth” In: *APL Photon* (2019).
- [21] Goodman, J.W. Introduction to Fourier Optics, 2nd ed.; McGraw-Hill, Inc.: New York, NY, USA, 1996; pp. 74–75.
- [22] Shi Zhao et al “All-Solid-State Beam Steering via Integrated Optical Phased Array Technology” In: *micromachines* (2022)
- [23] X. Qiang et al “ Large-scale silicon quantum photonics implementing arbitrary two-qubit processing” In: *Nature Photonics* (2018)
- [24] J Wang et al “Multidimensional quantum entanglement with large-scale integrated optics” In: *Science* (2018)
- [25] Yong Liu et “Silicon optical phased array with a 180-degree field of view for 2D optical beam steering” In: *Optica* (2022).
- [26] M.C. Estevez et al “Integrated optical devices for lab-on-a-chip biosensing applications” In: *Laser Photonics Rev.* (2012)
- [27] G B. Loozen et al “ Integrated photonics multi-waveguide devices for optical trapping and Raman spectroscopy: design, fabrication and performance demonstration” In: *Beilstein J. Nanotechnol* (2020)
- [28] D. Conteduca et al “Exploring the Limit of Multiplexed Near-Field Optical Trapping” In: *ACS Photonics* (2021).

- [29] R. J. Niffenegger et al “Integrated multi-wavelength control of an ion qubit” In: *Nature* (2020).
- [30] K. K. Mehta et al “Integrated optical multi-ion quantum logic” In: *Nature* (2020).
- [31] L. Bundalo *et al.*, "PIXAPP Photonics Packaging Pilot Line – Development of a Silicon Photonic Optical Transceiver With Pluggable Fiber Connectivity," In: *IEEE Journal of Selected Topics in Quantum Electronics* (2022)
- [32] P. Dong et al “Silicon photonic devices and integrated circuits,” In : *Nanophotonics* (2014).
- [33] T. Komljenovic *et al.*, “Heterogeneous silicon photonic integrated circuits,” In *J. Lightw. Technol* (2016).
- [34] D. Marris-Morini *et al.*, “Germanium-based integrated photonics from near- to mid-infrared applications,” In : *Nanophotonics* (2018).
- [35] M. Smit et al “Past, present, and future of INP-based photonic integration,” In: *APL Photon* (2019).
- [36] Sharma *et al.*, “Review of recent progress on silicon nitride-based photonic integrated circuits,” In: *IEEE Access*, (2020).
- [37] P. O’Brien et al , “Packaging of silicon photonic devices,” In: *Topics Appl. Phys* (2016)
- [38] L. Carroll *et al.*, “Photonic packaging: Transforming silicon photonic integrated circuits into photonic devices,” In: *Appl. Sci* (2016)
- [39] J. S. Lee *et al.*, “Meeting the electrical, optical, and thermal design challenges of photonic-packaging,” In: *IEEE J. Sel. Top. Quantum Electron* (2016).
- [40] C. Li *et al.*, “Silicon photonics packaging with lateral fiber coupling to apodized grating coupler embedded circuit,” In: *Opt. Exp* (2014).
- [41] N. Pavarelli *et al.*, “Optical and electronic packaging processes for silicon photonic systems,” In: *J. Lightw. Technol.* (2015)
- [42] B. Snyder et al , “Packaging process for grating-coupled silicon photonic waveguides using angle-polished fibers,” In: *IEEE Trans. Compon.,Packag. Manuf. Technol* (2013)
- [43] <https://www.nscrypt.com/precision-micro-dispensing/>

- [44] A S Putra et al “Microdispensing system via the contacting method” In: *ISA Transactions (2010)*
- [45] S.H. Eom et al , “Close-packed hemispherical microlens arrays for light extraction enhancement in organic light-emitting devices”, In: *Org. Electron (2011)*
- [46] E. Wrzesniewski et al., “Enhancing light extraction in top-emitting organic light-emitting devices using molded transparent polymer microlens arrays”, In: *Small 8 (2012)*.
- [47] Y.H. Ho et al. “Enhanced light outcoupling of organic light-emitting diode using metallic nanomesh electrodes and microlens array”, In: *Opt. Express (2013)*.
- [48] V. Lin et al. “Design and fabrication of long-focal-length microlens arrays for Shack-Hartmann wavefront sensors”, In: *Micro Nano Lett. (2011)*.
- [49] J.Y. Hu et al “Semi-ellipsoid microlens simulation and fabrication for enhancing optical fiber coupling efficiency”, In: *Sens. Actuators (2008)*
- [50] K. Kurihara et al, “Design and fabrication of microlens array for near-field vertical cavity surface emitting laser parallel optical head”, *Opt. Rev. (2003)*
- [51] Li Wang et al “Fabrication of microlens array with controllable high NA and tailored optical characteristics using confined ink-jetting” In: *Applied Surface Science (2018)*
- [52] Shaoliang Yu et al “Optical Free-Form Couplers for High-density Integrated Photonics (OFFCHIP): A Universal Optical Interface” In: *JOURNAL OF LIGHTWAVE TECHNOLOGY (2020)*.
- [53] S. M. Zia Uddin et al. “Micro-dispenser-based optical packaging scheme for grating couplers” In: *Optics Letters (2023)*.
- [54] Optical Communication Band  
<https://www.fiberlabs.com/glossary/optical-communication-band/>
- [55] High bit rate DWDM fronthaul, Ericsson blog.
- [56] Zi Wang et al “On-chip wavefront shaping with dielectric metasurface” In: *Nature Communications (2019)*
- [57] N. Na et al “Efficient broadband silicon-on-insulator grating coupler with low

- backreection.” *Optics letters*, (2011).
- [58] Yi Zhang et al.” Silicon multi-project wafer platforms for optoelectronic system integration” In: *IEEE International Conference* (2012).
- [59] Attila Mekis et al. “Scaling cmos photonics transceivers beyond 100 gb/s”. In: *SPIE OPTO (2012)*
- [60] Xiaochuan Xu et al “ Cmos compatible subwavelength grating couplers for silicon integrated photonics”. In: *Photonics Conference* (2012).